



Turbulence scale and strength analysis in the roughness and inertial sublayers over urban areas: A wind tunnel study

Fei Li ^a, Ruiqi Wang ^a, Guoliang Chen ^a, Ziwei Mo ^{b,c}, Naoki Ikegaya ^d, Chun-Ho Liu ^{a,*}

^a Department of Mechanical Engineering, The University of Hong Kong, 7/F, Haking Wong Building, Pokfulam Road, Hong Kong Special Administrative Region, China

^b School of Atmospheric Sciences, Sun Yat-sen University, Southern Marine Science and Engineering Guangdong Laboratory (Zhuhai), China

^c Key Laboratory of Tropical Atmosphere-Ocean System, Ministry of Education, Zhuhai, China

^d Faculty of Engineering Sciences, Kyushu University, 6-1 Kagugakoen, Kasuga, Fukuoka 816-8580, Japan

ARTICLE INFO

Keywords:

Amplitude modulation (AM)
Empirical mode decomposition (EMD)
Momentum transport
Quadrant-hole analysis
Real urban morphology
Turbulence scale

ABSTRACT

The dissimilarity of dynamics and turbulence structures between the roughness and inertial sublayers (RSL, ISL) over roughness elements show that ISL turbulence is much more homogeneous. Conventional logarithmic law of the wall is merely applicable for the RSL mean-wind-speed profiles. To characterize the turbulence scales and elucidate the mechanism, the flows in the atmospheric surface layer (ASL) over real urban morphology are measured in wind tunnel experiments fabricated by 3D-printing, reduced-scale model of downtown Kowloon Peninsula, Hong Kong. Elevated dispersive flux at urban canopy signifies the influence from individual buildings and inhomogeneous RSL flows. A positive momentum contribution appears in the low-frequency regime. The large-scale turbulence in RSL thus enhances the mixing and transport, resulting in inhomogeneous flows. The contribution from ejection Q2 and sweep Q4 increases and decreases, respectively, with increasing RSL motion strength. The conventional $-5/3$ law is observed by empirical mode decomposition (EMD) and the largest amplitude fluctuation occurs more often when the turbulence length scale is comparable to the turbulent boundary layer (TBL) thickness. The single-point amplitude modulation (AM) shows that the large- and small-scale turbulence correlates tightly at the bottom of RSL. Besides, the joint probability density function (JPDF) illustrates that accelerating large scales often occur with decelerating small scales, and they are intensified with increasing wall-normal distance. As a result, large-scale turbulence influences substantially the flow structures over urban areas and the small-scale turbulence (even) in RSLs in the vicinity of building obstacles.

1. Introduction

Street-level ventilation and pollutant removal in cities are some of the most concerned problems nowadays due to the large number of urban inhabitants. Especially, abundant vehicular exhaust would degrade pedestrian-level air quality more seriously in street canyons because of poor ventilation and weakened dispersion [1,2]. Therefore, an advanced understanding of transport mechanism is essential for refined air quality management and strategy, safeguarding public health.

Transport processes in the atmospheric surface layer (ASL) are important because pollutant dispersion is driven by winds and turbulence. In response to the aerodynamic resistance of individual buildings, a roughness sublayer (RSL) is developed immediately over urban canopy and below the (conventional) inertial sublayer (ISL). ASL flows exhibit distinct dynamics in RSL and ISL [3,4]. ISL dynamics are relatively homogeneous whose flux-gradient relationship is described well by the Monin-Obukhov similarity theory (MOST) [5]. Whereas, MOST is

merely applicable to RSLs with inhomogeneous dynamics so the mean-wind-speed profiles no longer follow the conventional logarithmic law of the wall (log-law) [6,7]. Instead, an empirical solution to ASL mean-wind speed was developed for both RSL and ISL [8–10]. These dissimilarities would influence ASL transport and the atmospheric modeling applications over urban areas in practice.

Previous works have focused on the influence of urban morphology and natural terrain on turbulence statistics or scalar transport [11–14]. Various aspects, such as thermal stability, advection, integral length and time scales, or budgets of TKE and heat, have been studied to quantify turbulence statistics for real, inhomogeneous urban street canyons [15,16]. Whilst, a fundamental understanding of the inhomogeneous RSL dynamics over urban areas is still indispensable. Recently, some studies have reported that large-scale turbulence coherence would modify the near-wall flows [17–19]. Besides, predictive models have been proposed based on scale interaction [20,21].

* Corresponding author.

E-mail address: liuchunho@graduate.hku.hk (C.-H. Liu).

Table 1
Categories of quadrant events.

Quadrants	Events	u''	w''
Q1	Outward interaction	+	+
Q2	Ejection	+	-
Q3	Inward interaction	-	-
Q4	Sweep	-	+

Moreover, turbulence intensity $u_i'' u_i''$ is another indicator for transport processes. Here, double-prime $\phi'' (= \phi - \langle \bar{\phi} \rangle)$, overbar $\bar{\phi}$, and angle bracket $\langle \phi \rangle$ denote the fluctuation, time average, and spatial average, respectively. A traditional method to quantify the contribution of turbulent momentum fluxes $u_i'' u_j''$ from different directions is quadrant analysis [22,23]. Among the four events (Table 1), ejection Q2 and sweep Q4 dominate vertical momentum transport $u'' w''$ [24].

Further to quadrant analysis, quadrant-hole analysis was proposed to partition turbulence motions according to their strength by a “hole” with designate sizes [25–28]. The momentum transport driven by diversified motion strength are important to elucidate pollutant dispersion. Applying the quadrant-hole analysis over vegetation-canopy models in wind tunnel experiments, the surface configuration (i.e. drag) poses a notable influence on RSL flows in which ejection Q2 and sweep Q4 are strengthened with increasing surface roughness [29,30]. Analyzing the large-eddy simulation (LES) results over urban areas instead, it was also found that the critical turbulence motion strength, which is most efficient in term of transport, is about 4 times larger than the average vertical momentum flux [31].

Apart from wind tunnel experiments and LES, field measurements have been collected to address the same concern. By monitoring the surface drag in typhoons or cold fronts, it was found that the momentum flux from ejection Q2 and sweep Q4 at high wind speeds decreases when the conditional sampling threshold hole size is smaller than 20 [32]. Likewise, it was observed from the ASL flows within and over a corn canopy that increasing hole size promotes the stress contribution from ejection Q2 and sweep Q4 [33]. Hence, the dominant events, ejection Q2 and sweep Q4, are strongly influenced by the motion strength over canopies. Their subsequent effect on street-level ventilation, however, has not yet been examined in details.

ASL turbulence structures were first investigated by experiments and simulations of the flows over smooth walls [34,35]. Apart from the momentum flux at different motion strength, turbulence scales influence the transport processes. In full-spectrum, fully developed turbulent flows, the scale could be as large as 20 times of the thickness of turbulent boundary layer (TBL) δ [36,37]. In particular, large-scale motions (LSMs) of turbulent flows with streamwise wavelength $\lambda_x \approx 10\delta$ have been observed recently [38–40]. Those large-scale packets carry over a quarter of the total momentum flux though they occupy less than 4% of the total area of vector field [41]. Besides, it was observed that large-scale structures account for more than half of the energy of streamwise velocity component [42]. The very large-scale motions (VLSMs; $\lambda_x \geq 20\delta$) were also identified in near-wall region [43].

LSMs and VLSMs collectively contribute to momentum flux, affecting the local dynamics [44,45]. To partition the contribution of momentum flux and turbulence kinetic energy (TKE), empirical mode decomposition (EMD) is another emerging tool to decompose (time trace of) turbulence according to length scales. It has been actively employed in analyzing non-linear, non-stationary phenomena in mechanical engineering [46] as well as weather forecast [47,48]. In fluid mechanics, EMD is efficient to separate the scales in a time series to investigate turbulence intermittency by which the conventional Kolmogorov spectrum and the characteristic turbulence ranges were successfully identified [49–51]. In view of its remarkable functionality, EMD is adopted in this paper.

Those LSMs and VLSMs resided in logarithmic regions were revealed by high-Reynolds-number experiments and simulations [52]. Their momentum transport is more efficient than that of small-scale structures due to the substantial TKE portion [42]. It was first reported over a decade ago that the small-scale structures in near-wall region are driven by LSMs via amplitude modulation (AM) [53]. The positive and negative velocity fluctuations of LSMs would accelerate and decelerate their small-scale counterparts, respectively. In addition to small scales, hot-wire anemometry (HWA) showed that dissipative scales in near-wall regions are modulated by LSMs [54]. Although tremendous works have been sought, most AM studies available in the literature have focused on the turbulence over either smooth walls or arrays of idealized roughness elements only. The scale interaction over real, heterogeneous urban morphology is not yet explored.

In this study, a series of wind tunnel experiments for the flows and turbulence over real urban morphology are conducted to examine the inhomogeneous RSL dynamics systematically. To demystify the inhomogeneity in the turbulence-scale perspective, a low-pass filter is adopted to process the velocity signals to contrast the momentum contribution at different cut-off frequencies. In the light of the (noticeable) influence from LSMs on RSL dynamics, the motion scales based on real urban morphology are examined by EMD. Their interaction is then analyzed by AM.

The structure of this paper is as follows. Section 2 introduces the theory related to ASL turbulence scales. The analytical methods adopted in this paper and the wind tunnel experiments are detailed in Section 3. Afterward, Section 4 discusses the characteristic turbulence and transport processes over real urban morphology together with the scale interactions. Finally, conclusions are drawn in Section 5.

2. Theoretical background

2.1. Quadrant-hole analysis

Air masses are classified into four events, namely Q1: outward interaction ($+u'', +w''$), Q2: ejection ($-u'', +w''$), Q3: inward interaction ($-u'', -w''$), and Q4: sweep ($+u'', -w''$) of vertical turbulent momentum flux $u'' w''$ according to their streamwise u'' and vertical w'' fluctuating velocities (Table 1). Here, + and – denote accelerating and decelerating flows, respectively.

Quadrant-hole analysis is further introduced by applying a hypothetical hole of size

$$\mathcal{H} = \frac{|u'' w''(t)|}{|u'' w''(t)|} \quad (1)$$

to the (magnitude of) momentum flux at time t (see Fig. 1). The contribution from different quadrants Q_i and motion strength $|u'' w''|$ to the total momentum flux $u'' w''$ is then measured by the conditional flux fraction

$$S_{i,\mathcal{H}} = \frac{\overline{u'' w''(t) \times F_{i,\mathcal{H}}}}{\overline{u'' w''(t)}}. \quad (2)$$

Here,

$$F_{i,\mathcal{H}}(u'', w'') = \begin{cases} 1, & \text{if } (u'', w'') \text{ lies in } Q_i \text{ and } |u'' w''| \geq \mathcal{H} \sqrt{u'' w''} \\ 0, & \text{otherwise} \end{cases} \quad (3)$$

is the condition function and $i (= 1, 2, 3, \text{ or } 4)$ the quadrant number [55,56]. Obviously, $S_{2,\mathcal{H}}$ and $S_{4,\mathcal{H}}$ are positive while $S_{1,\mathcal{H}}$ and $S_{3,\mathcal{H}}$ are negative.

Analogously, the time fraction of Q_i with motion strength $|u'' w''|$ is

$$T_{i,\mathcal{H}} = \frac{F_{i,\mathcal{H}}(u'', w'')}{\sum_{i=1}^4 F_{i,\mathcal{H}=0}(u'', w'')} \quad (4)$$

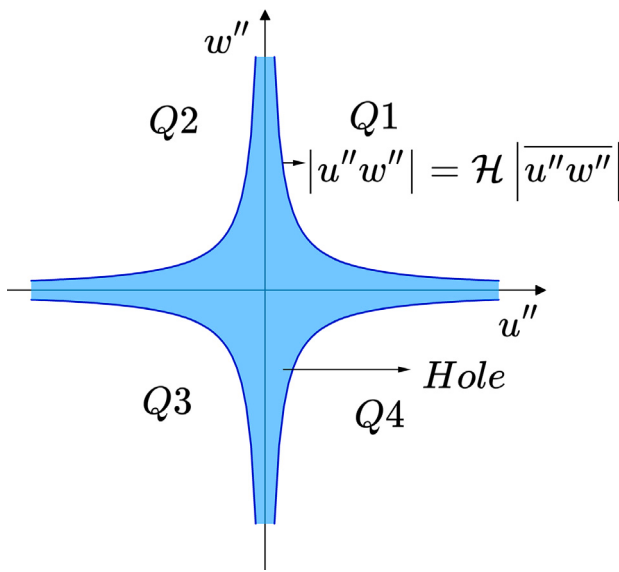


Fig. 1. Schematic of quadrants Q_i and quadrant-hole analysis.

where $\sum_{i=1}^4 \mathcal{F}_{i,H=0}(u'', w'')$ in fact is the total number of events of all the four quadrants. The difference in time fraction

$$\Delta\mathcal{T}_H = \mathcal{T}_{4,H} - \mathcal{T}_{2,H} \quad (5)$$

compares the importance between sweep Q4 and ejection Q2.

The exuberance

$$\eta_{ex} = \frac{S_{1,H} + S_{3,H}}{S_{2,H} + S_{4,H}} \quad (6)$$

is widely adopted to capture turbulence coherent structures and measure the transport efficiency [31,32]. Momentum transport is more efficient with less negative η_{ex} .

2.2. Empirical Mode Decomposition (EMD)

The original signal time trace $\phi(t)$ can be decomposed into a finite number N of oscillatory modes, which are called intrinsic mode functions (IMFs), with different characteristic frequencies f_i . IMFs have two properties. In the whole time trace, the number of extrema and zero-crossing are equal or differs at most by one. In addition, it has a zero-mean envelope defined by the local maxima and minima. Unlike simple harmonic function or Fourier transform, the amplitude $A_i(t)$ and frequency $f_i(t)$ of IMFs vary in time.

The one-dimensional (1D) time-series data are decomposed by EMD in this paper. The raw signal data ϕ are finally written as the sum of IMFs I_i and the residual R .

$$\phi(t) = \sum_{i=1}^N I_i(t) + R(t) . \quad (7)$$

After EMD, each IMF time series is processed by Hilbert spectral analysis (HSA) associated with its Hilbert transform to determine the instantaneous frequency $f_i(t)$ and instantaneous amplitude $A_i(t)$ [57,58]. The joint probability density function (JPDF) $P(f, A)$ is then expressed in terms of the frequency f_i and amplitude A_i generated from the IMFs. The procedure of EMD and Hilbert transform is detailed in Appendix.

2.3. Amplitude Modulation (AM)

Single-point amplitude modulation (AM) measures the correlation between the large-scale component and the filtered envelope of the small-scale fluctuation. First of all, the time-trace signal of streamwise

fluctuating velocity $u''(t)$ is decomposed into large-scale u''_L and small-scale u''_S components by a low-pass filter whose cut-off wavelength λ_c is equal to the TBL thickness δ (corresponding frequency \bar{u}/δ). Here, the subscripts L and S denote the large (low-frequency) and small (high-frequency) scales collected after low-pass filtering, respectively. Hilbert transform and low-pass filtering are then applied on the small-scale fluctuations u''_S to develop the corresponding large-scale envelope $E_L(u''_S)$ which represents the amplitude of the small scales. Finally, the AM correlation coefficient

$$R_{AM}(\tau) = \frac{\overline{u''_L(t+\tau) E_L(u''_S(t))}}{\sqrt{\overline{u''_L^2(t+\tau)}} \sqrt{\overline{E_L^2(u''_S(t))}}} \quad (8)$$

is calculated as a function of time lag τ that measures the correlation between the filtered envelope of small-scale $E_L(u''_S)$ and the large-scale u''_L fluctuating velocities [53].

3. Methodology

3.1. Wind tunnel experiment

A typical built environment mixed with both residential and commercial buildings in the downtown Kowloon Peninsula, Hong Kong Special Administrative Region (HKSAR), China, is selected as the modeling area. A reduced-scale model (1: 1,200) is fabricated by 3D-printing. It is 2 m (length) \times 0.55 m (width) with respect to the 3.6 km (length) \times 0.5 km (width) urban morphology in true scale. The actual mean building height in the measurement region is 36 m (true scale) corresponding to the mean building model height h_m ($= 30 \times 10^{-3}$ m) of the urban model. Real urban morphology is used in this paper to complement our previous findings based on idealized urban morphology [59].

The experiments are carried out in the wind tunnel in the Department of Mechanical Engineering, The University of Hong Kong (Fig. 2a) [3,8,10,30,60]. The test section, which is made of acrylic, is 6 m (length) \times 0.56 m (width) \times 0.56 m (height) and the maximum wind speed is 15 m s⁻¹. The freestream wind speed in this experiment is in the range of 8.8 m s⁻¹ $\leq U_\infty \leq$ 9.6 m s⁻¹ and the friction velocity is 0.62 m s⁻¹ $\leq u_r \leq$ 0.67 m s⁻¹. The TBL thickness δ over the urban model is defined at the height z where the ensemble-averaged wind speed converges to 99% of the freestream one $\langle \bar{u} \rangle|_z = 0.99U_\infty$ which is around 180×10^{-3} m. The spatio-temporal average $\langle \bar{\phi} \rangle$ is regarded as the ensemble average. According to the freestream wind speed U_∞ and the TBL thickness δ , the Reynolds numbers $Re_\infty (= U_\infty \delta / v)$ and $Re_r (= u_r \delta / v)$ are around 170×10^3 and 12×10^3 , respectively, that is sufficiently large for fully developed turbulent flows independent from Reynolds number [61].

Three parallel (vertical x - z) planes, which are denoted as 1st, 2nd, and 3rd, are assigned as the measurement planes. To avoid the influence from the side walls, the 2nd plane is aligned along the centerline of real-urban model and wind tunnel, and the 1st and 3rd planes are assigned beside the 2nd plane with a short distance of 100×10^{-3} m apart (Fig. 2b). The clearance is thus kept at least 150×10^{-3} m to the side walls of the wind tunnel to avoid excessive end-wall effect. The 1st and 3rd planes are also selected based on the different mean building height to contrast the influence of surface roughness.

3.2. Flow sampling and data acquisition

Being controlled by a transverse system, 46 sampling locations are evenly spaced on each plane in the streamwise x direction to measure the vertical velocity profiles ($\Delta x = 10 \times 10^{-3}$ m). Along each profile, 96 sampling points are assigned at wall-normal distance 5×10^{-3} m $\leq z \leq 255 \times 10^{-3}$ m above the tallest building model (whose height $h_{max} = 60 \times 10^{-3}$ m).

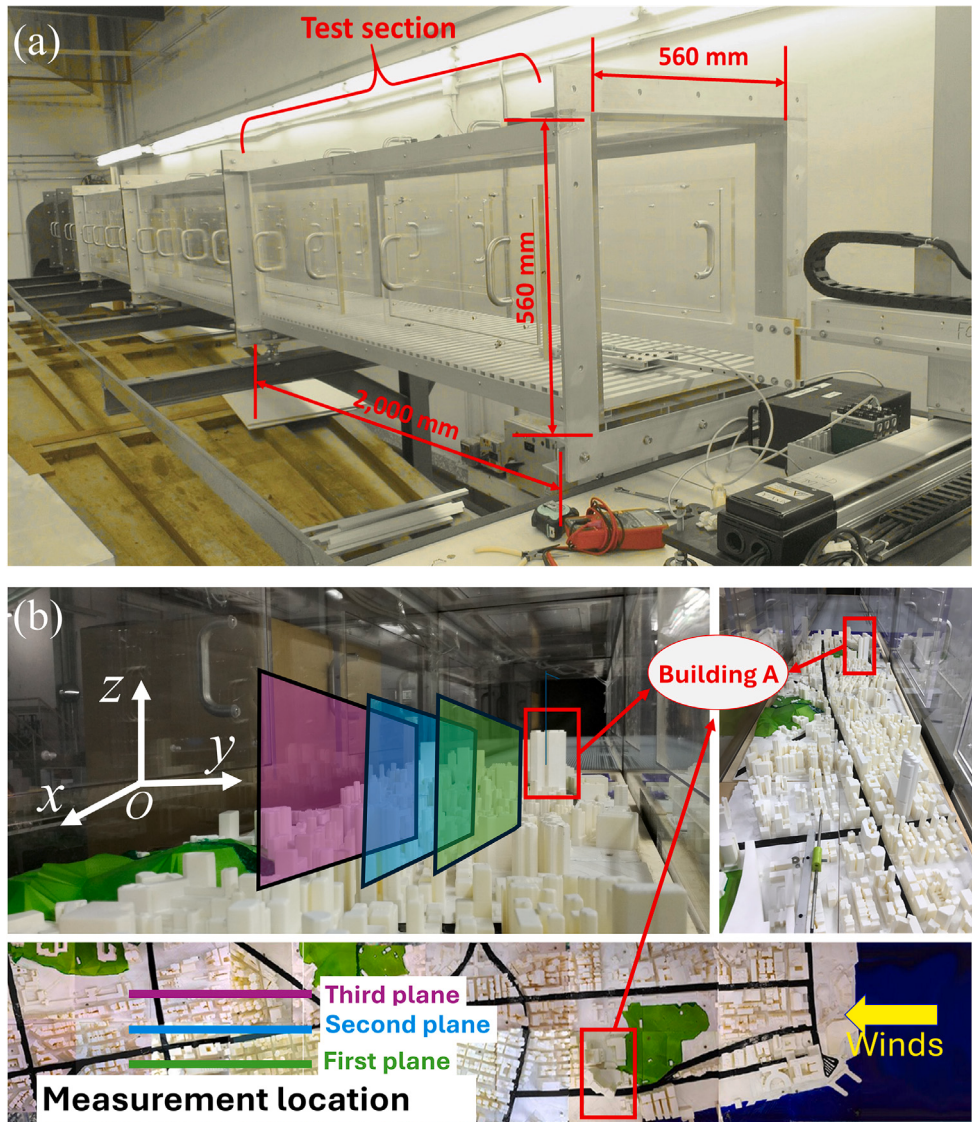


Fig. 2. (a) Wind tunnel facility and (b) reduced-scale urban model. Also shown are the dimensions and the measurement locations/planes.

Constant temperature (CT) hot-wire anemometer (HWA) with a X-wire design is adopted to measure the streamwise u and vertical w velocities. These two velocity components play key roles in the transport processes over urban canopy so the spanwise velocity v is not considered in this paper. The CT HWA probe consists of a pair of 5-μm diameter tungsten wires with platinum-plated surface. The 2-mm active length of the platinum-plated tungsten wires is fabricated by copper electroplating. The included angle between the X-wire pair is 100° ($\geq 90^\circ$) to improve the accuracy.

Some key parameters of aerodynamics and TBL of the three planes in the wind tunnel experiments are tabulated in Table 2. The zero-plane displacement d and roughness height z_0 are determined by the log-law

$$\langle \bar{u} \rangle = \frac{1}{\kappa} \ln \frac{z - d}{z_0} \quad (9)$$

in the ISL where κ (= 0.4 in this paper) is the von Kármán constant, $\langle \bar{u} \rangle$ the ensemble-averaged mean streamwise velocity, u_τ the friction velocity, and z the height. The range of ISL is determined by the largest momentum flux with a 10% tolerance [10]. It is assumed that the ISL bottom is the RSL top. The friction velocity u_τ ($= \left(-\langle u'' w'' \rangle \right|_{z=h} \right)^{1/2}$) is calculated by the vertical turbulent momentum flux [8,9]. Molecular shear is neglected because of the large Reynolds number [10].

4. Results and discussion

4.1. Mean flow and turbulence

To characterize the turbulence over the urban model, the ensemble-averaged wind speed $\langle \bar{u} \rangle$, streamwise $\langle u'' u'' \rangle^{1/2}$ and vertical $\langle w'' w'' \rangle^{1/2}$ fluctuating velocities, together with vertical momentum flux $\langle u'' w'' \rangle$ on the three measurement planes are examined (Fig. 3). All the variables are normalized by the friction velocity u_τ ($= \left(-\langle u'' w'' \rangle \right|_{z=h} \right)^{1/2}$) at the canopy level [62,63]. It is noticeable that there exists major flow inhomogeneity in response to individual building blocks in the RSLs $0 \leq z \leq 0.4d$ on the 1st plane.

On the 1st plane, the RSL mean-wind speed $\langle \bar{u} \rangle$ increases in the streamwise direction from $6u_\tau$ to $10u_\tau$. Besides, the wind shear $d \langle \bar{u} \rangle / dz$ is abrupt in the lower RSL but is mild in the upper RSL. The high-rise Building A upstream the 1st plane is the major reason (Fig. 2b).

On the contrary, the vertical profiles of flow variables on the 2nd and 3rd planes do not have large variations because of the mild surface roughness. In view of the surface heterogeneity, the downward momentum flux $\langle u'' w'' \rangle$ on the 1st plane shows an obvious difference

Table 2
Aerodynamics and turbulent boundary layer (TBL) parameters of the three measurement planes [10].

		1st plane	2nd plane	3rd plane
Mean building height ($\times 10^{-3}$ m)	h_m	37 ± 19	27 ± 15	26 ± 16
Free-stream velocity (m s $^{-1}$)	U_∞	8.86 ± 0.57	9.62 ± 0.61	9.59 ± 0.69
Friction velocity (m s $^{-1}$)	u_τ	0.67 ± 0.04	0.62 ± 0.01	0.65 ± 0.01
Turbulent boundary layer (TBL) thickness ($\times 10^{-3}$ m)	δ	185 ± 6	178 ± 8	180 ± 8
Roughness length ($\times 10^{-3}$ m)	z_0	1.2 ± 0.5	0.9 ± 0.3	1.1 ± 0.4
Zero-plane displacement ($\times 10^{-3}$ m)	d	25 ± 6	24 ± 4	37 ± 5
Roughness sublayer top ($\times 10^{-3}$ m)	RSL top	78 ± 6	74 ± 5	76 ± 4
Inertial sublayer thickness ($\times 10^{-3}$ m)	ISL thickness	27	26	22
Reynolds number	$Re_\infty = U_\infty \delta / \nu$	1.7×10^5		
	$Re_\tau = u_\tau \delta / \nu$	1.2×10^4		

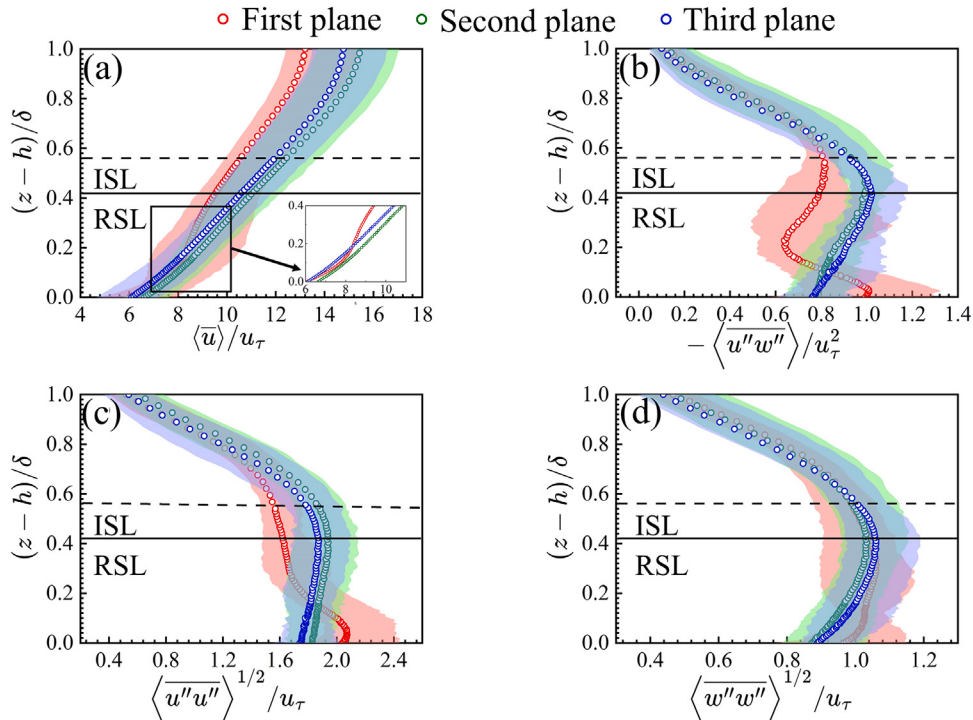


Fig. 3. Ensemble averaged vertical profiles of (a) mean-wind speed $\langle \bar{u} \rangle$; (b) vertical momentum flux $\langle \bar{u''w''} \rangle$; (c) streamwise velocity fluctuation $\langle \bar{u''u''} \rangle^{1/2}$; and (d) vertical velocity fluctuation $\langle \bar{w''w''} \rangle^{1/2}$ on the three planes. The corresponding variations on each plane are shaded accordingly.

compared with that on the other two planes (Fig. 3b). The momentum flux maxima occur in the ISLs [64,65]. The streamwise fluctuating velocity $\langle \bar{u''u''} \rangle^{1/2}$ on the 1st plane keeps decreasing with increasing height. Whilst, it exhibits an increasing trend in the RSL that is peaked in the ISLs on the 2nd and 3rd planes (Fig. 3c). On all the three planes, the vertical fluctuating velocity $\langle \bar{w''w''} \rangle^{1/2}$ increases first in the RSL then decreases thereafter whose maxima appear in the RSL-ISL interface (Fig. 3d).

4.2. Dispersive flux

Dispersive vertical momentum flux

$$\langle \bar{u''}\bar{w''} \rangle = \langle (\bar{u} - \langle \bar{u} \rangle)(\bar{w} - \langle \bar{w} \rangle) \rangle \quad (10)$$

is calculated based on the ensemble- and time-averaged flow properties to measure the spatial inhomogeneity on the three planes (Fig. 4). On the 1st plane, the dispersive momentum flux is peaked at around $z = 0.2\delta$. It is much larger than that on the other two planes (over fivefold) because of the elevated (25% higher) roughness length z_0 ($= 36 \times 10^{-3}$ m, 27×10^{-3} m, and 26×10^{-3} m on the 1st, 2nd, and 3rd planes, respectively). This finding also echos the abrupt RSL velocity gradient on the 1st plane discussed above.

The dispersive vertical momentum flux $\langle \bar{u''}\bar{w''} \rangle$ on the 2nd and 3rd planes is peaked at the RSL bottom. Obviously, it is much larger in the RSLs than that in the ISLs on all the three planes. Hence, the flow (spatial) variation is more intense in RSLs that is partly attributed to the sizeable building blocks. RSL dynamics heterogeneity would modify street-level transport processes [8,10,31] so it is worthy to elucidate the mechanism in terms of turbulence scales/strength in the upcoming sections.

4.3. Momentum transport scale

To analyze how the abrupt spatial variation and inhomogeneous flows in RSLs are influenced by turbulence scales, the fluctuating velocities u_i'' are processed by a low-pass filter (cut-off frequency f_c) to compare their contributions to momentum flux $u''w''$ at different frequencies (Fig. 5). Apparently, in the ISLs, the (very) low-frequency motions contribute negatively to the momentum flux, whereas the high-frequency motions contribute positively that eventually offset their low-frequency counterparts.

On the 1st plane, the contribution to momentum flux gradually increases from low- to high-frequency (Fig. 5a). The low-frequency motion scales contribute less negatively at the RSL bottom than do at

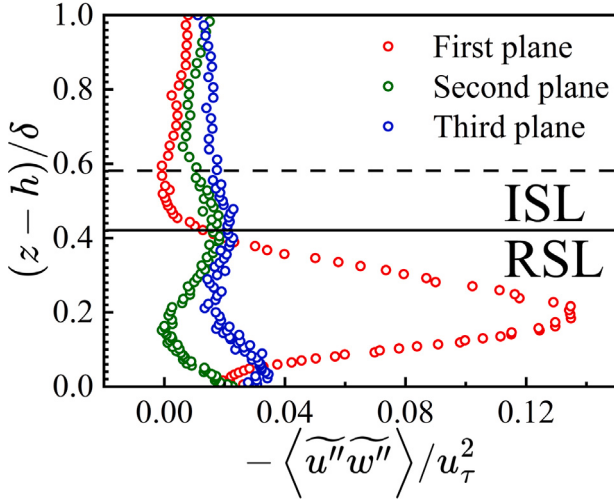


Fig. 4. Vertical profiles of dispersive turbulent vertical momentum flux $-\langle \tilde{u}'' \tilde{w}'' \rangle / u_\tau^2$ on the three planes.

higher levels. With increasing height, the negative momentum contribution from low-frequency motion scales enlarges. The least negative momentum contribution (from low frequencies) resides at the RSL bottom. Other than the RSLs, negative contributions from low-frequency motion scales to vertical momentum are observed on the 2nd (Fig. 5b) and 3rd (Fig. 5c) planes. Hence, the contribution from large scales to ISL momentum flux is marginal.

Down in the RSLs on the 2nd and 3rd planes, the large-scales motion contribute positively to the vertical momentum flux that is different from that on the 1st plane. The dissimilarity could be attributed to the very different dispersive momentum flux in response to surface heterogeneity among the three sets of urban morphology. It in turn evidences the influence of large-scale turbulence on the flows even at RSL bottom.

The inhomogeneous flows and inapplicability of the log-law in RSLs (turbulent transport cannot be modeled by anti-gradient diffusion) can be explained by turbulence scales. Besides, the contribution from eddies is in the range of dimensionless frequency $10^{-6} \leq f_c \delta / \langle \tilde{u} \rangle \leq 10^3$ (corresponding to $0.1 \text{ Hz} \leq f_c \leq 10 \text{ Hz}$) that decreases then increases thereafter with increasing the cut-off frequency f_c in the RSL bottom on the 2nd and 3rd planes. Hence, higher-frequency scales would intensify momentum fluxes from eddies.

4.4. Quadrant-hole analysis

Alike our previous work [10], the vertical momentum flux $u''w''$ over urban areas is dominated by Q2 and Q4. Whereas, how the momentum transfer is influenced by the hole size H , i.e. motion strength, is still unknown. As such, the momentum flux fraction $S_{i,H}$ contributing to the total momentum flux $\langle u''w'' \rangle$ from Q_i at different hole sizes H are calculated (Fig. 6).

The momentum flux contribution from Q1 and Q3 varies with height and motion strength (Fig. 6). Obviously, $S_{1,H}$ and $S_{3,H}$ are weakened with enlarging hole size H on all the three planes. On the 1st plane, there exists a bulge for Q1 and Q3 at around $(z-h)/\delta = 0.2\delta$ due to the upstream high-rise building (Building A in Fig. 2b) that concurs with the elevated dispersive momentum flux $\langle \tilde{u}'' \tilde{w}'' \rangle$ (Fig. 4). On the 2nd and 3rd planes, the momentum flux contribution from Q1 gradually decreases with increasing elevation at the same H but Q3 increases.

The magnitudes of contour gradient $|dS_{i,H}/dH|$ of Q1 and Q3 at $(z-h) = 0$ (RSL) and $(z-h) = 0.5$ (ISL) on the three planes are shown in Fig. 7a(i) and b(i), respectively. The gradients of Q1 and Q3 along H decrease rapidly in both the RSLs and ISLs. In the RSLs, the Q1 gradient

decreases more slowly than does Q3. Their attainable largest hole sizes (the gradient vanishes) are 10 and 5 for Q1 and Q3, respectively (Fig. 7a(i)). As such, accelerating updrafts are more sensitive to motion strength. In the ISLs, the gradients of Q1 and Q3 decrease similarly whose strongest motion scales are around 7 (Fig. 7b(i)).

Given the same hole size on all the three planes, $S_{2,H}$ increases with increasing elevation whose minimum resides at the RSL bottom. On the contrary, $S_{4,H}$ is peaked at the bottom of RSL then reduces with increasing height all the way from RSL to ISL and thereabove. This finding is consistent with that reported elsewhere [66]. Hence, it is suggested that Q4 sweep dominates RSL transport.

Those Q4 events on the 1st plane deserve elaboration (Fig. 6a(iv)). Fig. 7 shows the rate of change of momentum fraction $S_{4,H}$ with respect to hole size H at the RSL bottom ($z-h=0$). The variation of momentum fraction is largest at $H \approx 2$. The hole size of the largest motion strength falls within $22 \leq H \leq 25$ in the RSL bottom where the magnitude of contour gradient $|dS_{4,H}/dH|$ vanishes. It is in turn suggested that the momentum cannot be transported beyond this hole size. Moreover, sweep Q4 would diminish when the hole size H is greater than 25. Besides, there is an overall decreasing trend except for the bulge at $(z-h) = 0.2\delta$ due to the high-rise buildings (Building A in Fig. 2b).

In the ISL, the Q4 gradient is also peaked close to $H = 2$ on all the three planes. The strongest motion is found within $10 \leq H \leq 12$ (Fig. 7b(ii)). On the 2nd (Fig. 6b(iv)) and 3rd (Fig. 6c(iv)) planes, the trends are much smoother than those on the 1st plane. The variation trend of Q2 is opposite to that of Q4 (Fig. 6a(iii) to c(iii)). On the 1st plane (Fig. 6a(iii)), the largest hole size displays an overall increasing trend. There is also a bulge at $(z-h) = 0.2\delta$ due to the wake after a high-rise building (Building A in Fig. 2b). It is thus suggested that both Q2 and Q4 are strengthened by sizeable roughness elements. On the 2nd (Fig. 6b(iii)) and 3rd (Fig. 6c(iii)) planes, combined with the magnitude of contour gradient $|dS_{i,H}/dH|$ at the bottom of RSL ($z-h=0$; Fig. 7a(ii) and b(ii)), the hole sizes are as large as $10 \leq H \leq 12$ at the bottom of RSL and $18 \leq H \leq 20$ in ISL. Under this circumstance, ejection is being weakened gradually that eventually disappears when $H \geq 20$ at the bottom of RSL and $H \geq 25$ in ISL. The results above are consistent with those reported elsewhere [31].

4.5. Quadrant time fraction

Fig. 8 displays the difference in time fraction ΔT_H between sweep Q4 and ejection Q2 with different hole sizes H on the three planes at different height $(z-h)/\delta$. It illustrates the dominant event at different motion strength by comparing the difference between the contribution from Q4 and Q2 events. It gradually increases with enlarging hole size in RSLs, suggesting the strengthening motion scales. These phenomena are attributed to the increasing and decreasing contributions from sweep Q4 and ejection Q2 to momentum transport, respectively. The sweep Q4 dominates the large-motion-strength turbulence while the ejection Q2 is more important than Q4 for the weaker motion strength in RSLs. In this connection, it is suggested that accelerating downdraft is more frequent for pollutant transport when the motion strength is strong. On the other hand, decelerating updraft dominates the pollutant removal in the weak-motion-strength region in RSLs. However, the phenomenon is opposite in the ISL, where ΔT_H decreases with enlarging hole size H , suggesting that ejection Q2 plays a more important role than does sweep Q4 for weak motion strength in ISL. Hence, it is signified that decelerating updraft (accelerating downdraft) is more efficient for the momentum transport for stronger (weaker) motion strength in ISL.

4.6. Transport efficiency

Since both Q2 and Q4 are crucial for momentum transport, the ensemble average of momentum transport efficiency η_{ex} on each plane

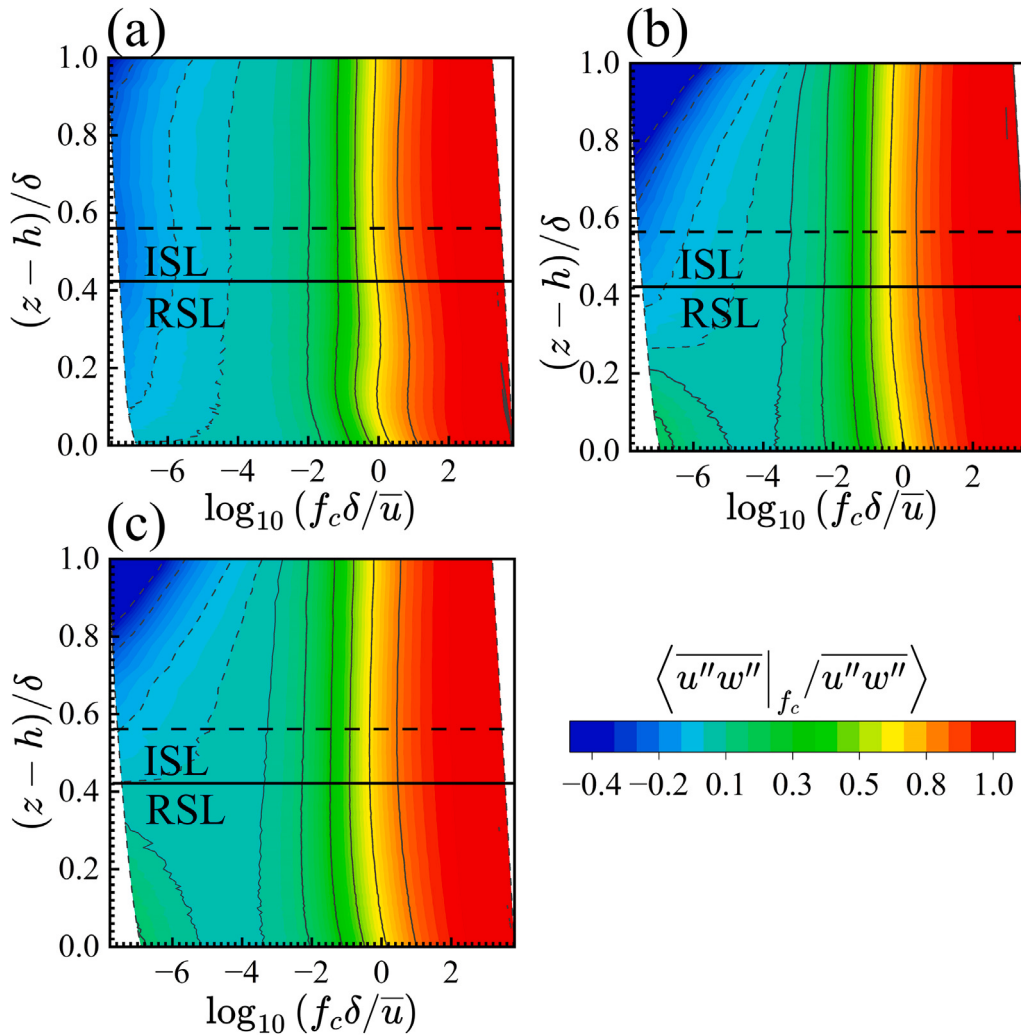


Fig. 5. Momentum flux contribution after low-pass filtering $\left\langle \overline{u''w''} \Big|_{f_c} / \overline{u''w''} \right\rangle$ at different cut-off frequency f_c on the (a) 1st; (b) 2nd; and (c) 3rd planes. The solid and dashed contour lines denote the positive and negative contributions, respectively.

over the urban areas is compared in Fig. 9 to investigate how the transport efficiency is influenced by different motion strength.

In both RSL and ISL, η_{ex} increases with the enlarging hole size H on all the three planes. The momentum transfer efficiency increases with intensifying motion scales. The exuberance η_{ex} is peaked in the ISL regardless of the motion strength. Hence, momentum transfer is most efficient in the ISLs right over buildings. On the 1st plane, there is a large area where displays least efficient momentum transfer in the ISL with small motions, which, however, is not found on the other two planes. It is mainly caused by the large variations of building blocks combined with the wake influence (Fig. 3).

4.7. EMD

EMD is useful to separate the scales of non-linear, non-stationary signal, characterizing the frequency. It partitions the original time series of velocity into 12 IMFs I_i and 1 residual term R in this study. Afterward, the power spectra density (PSD) $\Phi_{u''u''}$ is calculated for each IMF to identify the corresponding dominant scales. With increasing IMF order, the frequency of peaked PSD of each mode decreases, suggesting the enlarging turbulence motion scales (Fig. 10a to c). In this connection, I_1 to I_6 are obviously in the inertial subrange that align with the conventional $-5/3$ Kolmogorov spectrum for the dynamics.

On all the three planes, the peaked frequencies of pre-multiplied PSD of individual IMFs signify the corresponding integral motion scales (Fig. 10d to f). IMF5 contributes most energy whose turbulence scales dominate on all the three planes. The characteristic dimensionless frequency $f\delta/u_\tau$ is around 2 (corresponding to $f = 10$ Hz) that is about an eddy turnover across the TBL. Considering the Taylor hypothesis, the length scale of I_5 is about 200×10^{-3} m which is comparable to the TBL thickness of the wind tunnel experiments δ (185×10^{-3} m, 178×10^{-3} m, and 178×10^{-3} m on the 1st, 2nd, and 3rd planes, respectively). In view of the I_5 energy dominance, it is suggested that large-scale turbulence would influence the flow dynamics even at the bottom of RSL.

4.8. Hilbert-Huang spectrum

The relationship of fluctuating velocity u'' between amplitude A (turbulence strength) and frequency f (turbulence scale) can be described by EMD and Hilbert-Huang transform (HHT) in the amplitude-frequency domain. The JPDF $P(f, A)$ at $(z-h)/\delta = 0$ (RSL) and $(z-h)/\delta = 0.5$ (ISL) is displayed in Fig. 11. The black, filled circles denote the most likely occurring amplitudes of streamwise fluctuating velocity $|u''|$ at different frequencies. The ridge lines of JPDF shows an increasing trend with increasing frequency, arrive the maxima around $\lambda_x = \delta$, then drop thereafter. In both RSL and ISL on all the three planes, the

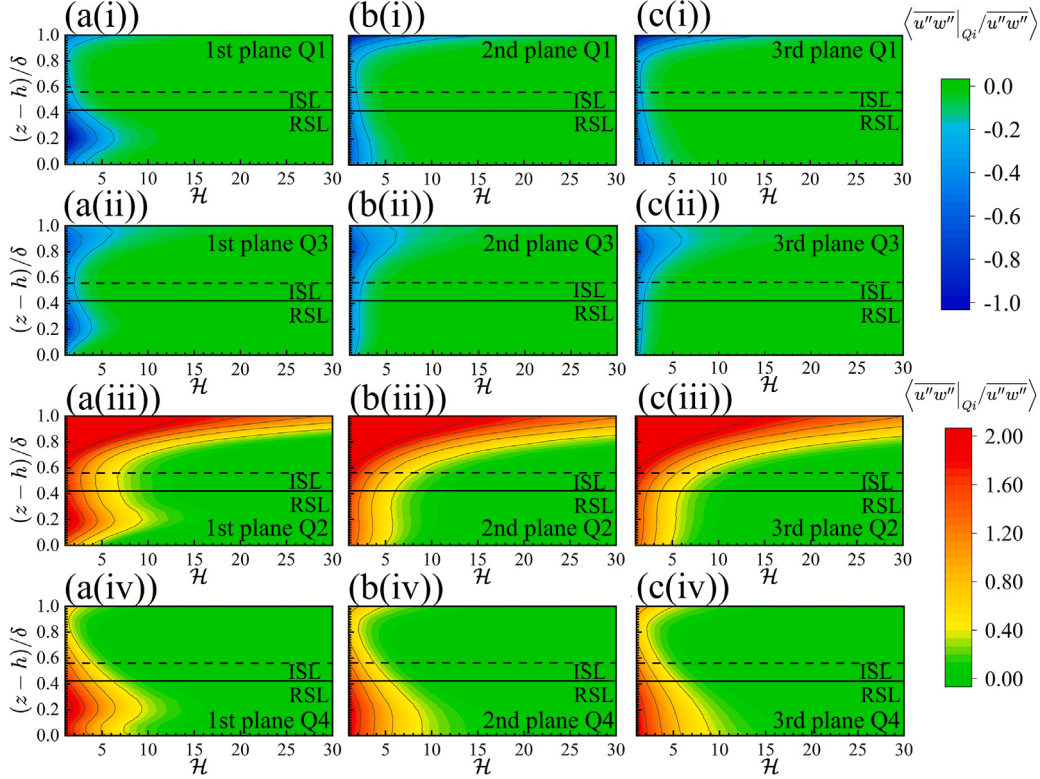


Fig. 6. Conditional momentum flux fraction of $S_{1,H}$ ((a(i)) ~ (c(i))), $S_{3,H}$ ((a(ii)) ~ (c(ii))), $S_{2,H}$ ((a(iii)) ~ (c(iii))), and $S_{4,H}$ ((a(iv)) ~ (c(iv))) at different hypothetical hole size H for the 1st (a(i)) ~ (a(iv)), 2nd (b(ii)) ~ (b(iv)), and 3rd (c(i)) ~ (c(iv)) planes. The solid and dash lines represent the RSL top and ISL top, respectively.

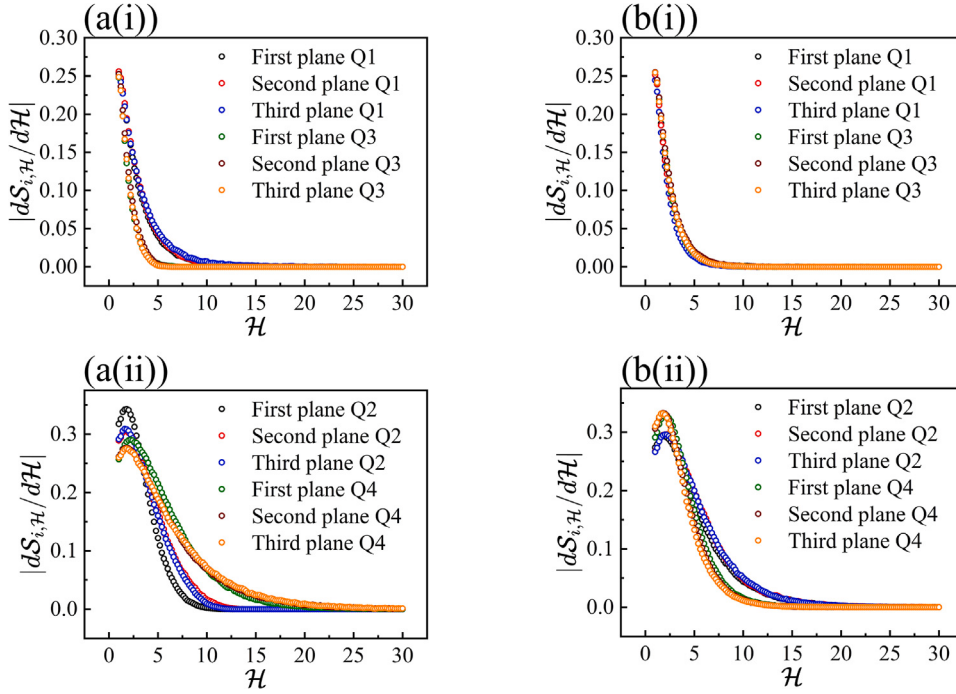


Fig. 7. Rate of change of $S_{i,H}$ with respect to the hole size H in Fig. 6 at (a) RSL bottom ($z - h)/\delta = 0$ and (b) ISL ($z - h)/\delta = 0.5$.

most frequent event with large fluctuating streamwise velocity u'' is found at the length scale λ_x close to the TBL thickness δ . The small- and very large-scale turbulence tends to occur with smaller amplitude and weaker turbulence strength. While the motion scales are dominated by the TBL-comparable ones, turbulence with the largest amplitude and length scale δ occurs more frequently.

4.9. Amplitude modulation

The frequency analysis evidences that the large-scale turbulence influences the flows, including small scales, even at the bottom of RSL in the vicinity of solid boundaries. To elucidate the interaction between large and small scales in the wall-normal direction, this section explores

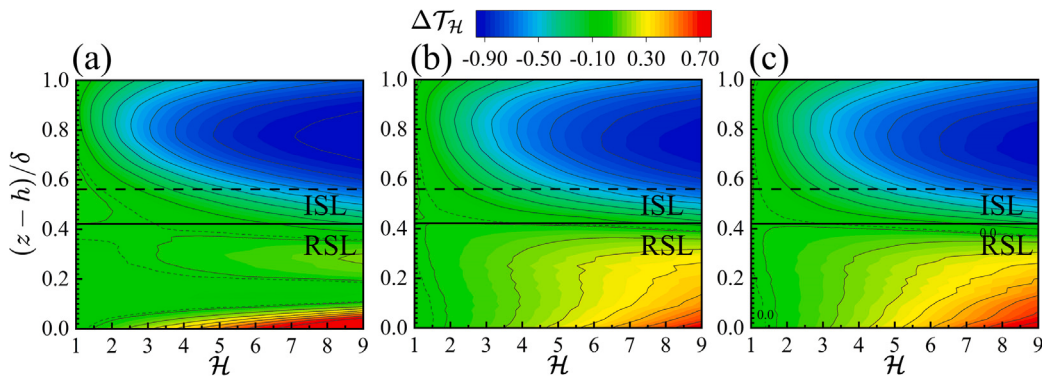


Fig. 8. Difference in time fraction ΔT_H expressed as functions of hole size H and height $(z - h)/\delta$ on the (a) 1st; (b) 2nd; and (c) 3rd planes. The solid and dashed lines denote the positive and negative contours, respectively.

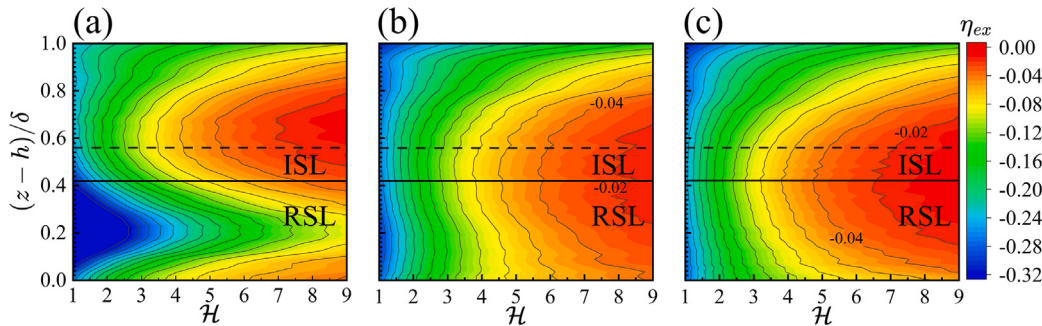


Fig. 9. Exuberance η_{ex} expressed as functions of hole size H and height $(z - h)/\delta$ on the (a) 1st; (b) 2nd; and (c) 3rd planes. The solid and dashed lines denote the positive and negative contours, respectively.

their AM based on the high-Reynolds-number experimental data in the ASL. From RSL to ISL, the AM correlation coefficient with zero time-lag $R_{AM}(\tau = 0)$ decreases with increasing height (Fig. 12). The largest, positive R_{AM} touches down at the RSL bottom. Hence, there exists a strong interaction between large- and small-scale turbulence even in the near-wall region, concurring the results reported in Section 4.3.

On all the three planes, there exists a zero-crossing (where $R_{AM} = 0$) at the RSL-ISL interface. The turbulence processes of large and small scales are thus nearly independent at that level. The switching of R_{AM} from positive to negative in the wall-normal direction has been also observed elsewhere [18,54]. In the RSL, the large- and small-scale turbulence is correlated positively so they are mostly accelerating or decelerating at the same time. Moreover, their coupling is peaked at the RSL bottom. On the contrary, the R_{AM} in ISL is negative so the small-scale turbulence is suppressed (enhanced) by the large-scale fast (slow) air masses.

The AM correlation coefficient R_{AM} effectively describes the interaction between large- and small-scale turbulence based on the assumption that the energy of small scales has a universal response to the large scales [21]. Fig. 13 shows the JPDF of u_L'' and $E_L(u_S'')$ at $(z - h)/\delta = 0$ (Fig. 13a ~ c; RSL) and $(z - h)/\delta = 0.5$ (Fig. 13d ~ f; ISL). It contrasts the likelihood for different events and evaluates the energy dependence between large and small scales. In the RSLs, Q1 and Q3 events occur frequently, dominating the flows on all the three planes (Fig. 13). The most likely occurring event appears in Q3 where $u_L'' < 0$ and $E_L(u_S'') < 0$. It is thus suggested that, at the bottom of RSL, the low-speed, large-scale fluctuations carry less small-scale energy while the high-speed, large-scale fluctuations occur with more energetic small-scale fluctuations frequently. While in the ISL, the JPDF is peaked in Q4 where the signs (directions) of large-scale u_L'' and small-scale $E_L(u_S'')$ turbulence are opposite, suggesting the suppression between them. Moreover, the events dominate in Q2 and Q4. In the ISL, the low-speed, large-scale fluctuations occur more frequently accompanying with more energetic,

small-scale fluctuations and the high-speed, large-scale fluctuations carry less small-scale energy.

From RSL to ISL, the quadrant positions of the peaked JPDF on the three planes vary (Fig. 14). With increasing height, the most frequent event moves from Q3 to Q4 during which the JPDF peak gradually approaching the coordinate origin. Hence, increasing the speed of large-scale turbulence structures with decreasing small-scale energy gradually dominates the flows.

The phase between large- and small-scale turbulence is not included in the analysis above though the phase shift between the large and small scales has been observed [67–70]. The AM correlation coefficients with varying phase lag τ between the large- and small-scale turbulence in the wall-normal direction (Eq. (8)) are depicted in Fig. 15. When $\tau u_\tau/\delta = 0$, R_{AM} is discussed previously (Fig. 12). R_{AM} is positive in the RSL. The positive peak of R_{AM} appears for $\tau u_\tau/\delta > 0$ across the RSL, suggesting that the small-scale fluctuations lead the large-scale fluctuations. With increasing height, the time lag $\tau u_\tau/\delta$ between the large- and small-scale increase from 0 to 0.015. A similar phenomenon has been reported elsewhere [54,69,71]. In-between the RSL and ISL, there is a zero zone where $R_{AM} = 0$, signifying that the turbulence intermittency influences the scale interactions, resulting in such scale arrangement [54,72].

In the ISLs, R_{AM} is negative so the large-scale fluctuations are negatively correlated with the small-scale ones. In this connection, the ridge lines in this region are asymmetrically converging to $\tau u_\tau/\delta = 0$ from ISL bottom to the TBL top. The ridge lines in ISL also turn negative, implying the negative phase lag between the two signals. Moreover, the large-scale turbulence leads its small-scale counterpart with the time lag $-0.02 \leq \tau u_\tau/\delta \leq 0.01$ which is around several sampling intervals.

5. Conclusions

In this paper, wind tunnel experiments over the reduced-scale physical model of real urban morphology are performed to contrast the

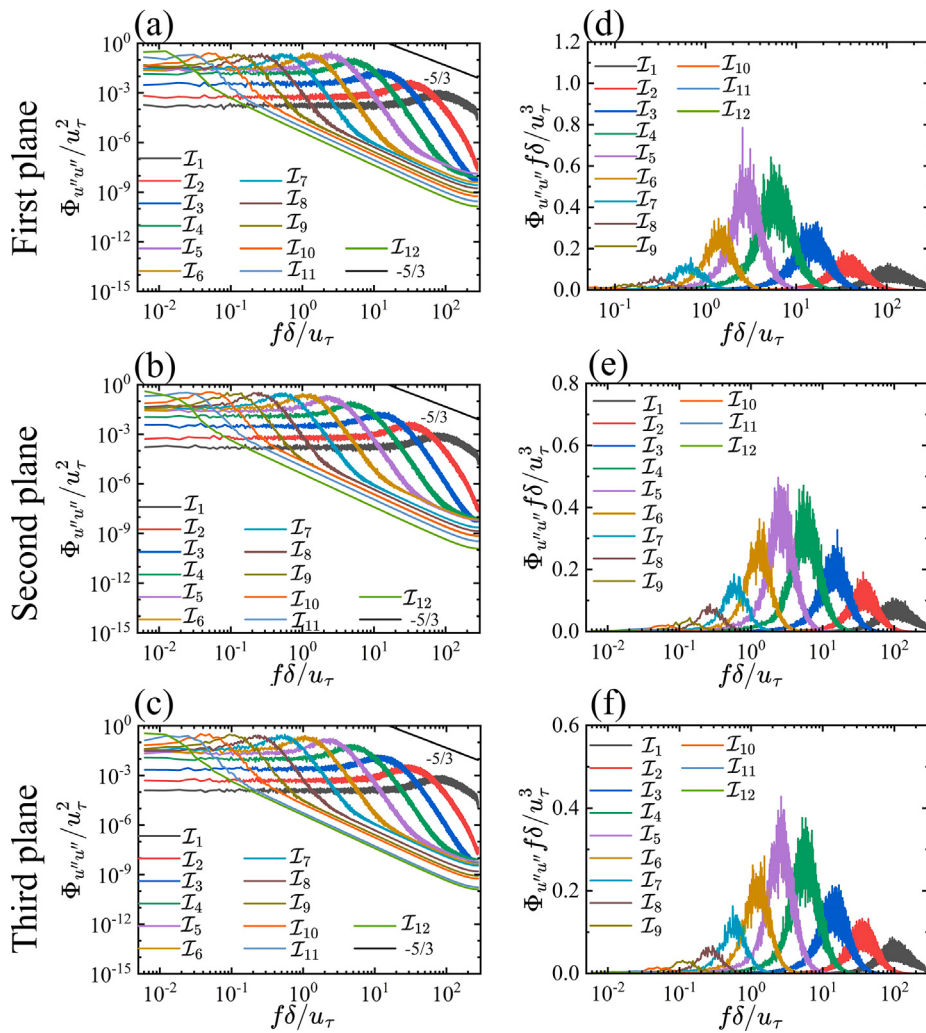


Fig. 10. Streamwise fluctuating velocity u'' PSD of ((a), (b), and (c)) and pre-multiplied PSD ((d), (e), and (f)) of the IMFs derived from EMD at $(z-h)/\delta = 0$ on the: (a) and (d) 1st; (b) and (e); 2nd; together with (c) and (f) 3rd planes.

multi-scale dynamics in ISLs and RSLs. Vertical profiles of winds and turbulence are measured by CT HWA on three (vertical) planes parallel to the streamwise direction to characterize RSL and ISL flows. Major findings are as follows:

1. Flow inhomogeneity is found in RSLs. The spatial variations of RSL streamwise velocity are quite substantial. The momentum contribution from large-scale turbulence decreases with increasing elevation. It influences the small scales in lower RSLs which subsequently intensifies RSL mixing, resulting in inhomogeneous flows.
2. The motion strength in RSLs and ISLs are dissimilar. The maximum motion strength increases (decreases) along with elevation for Q2 ejection (Q4 sweep). The momentum difference between Q2 and Q4 increases with enlarging hole size H in RSL, suggesting that Q4 dominates the large motion scales. The momentum transport efficiency is peaked in ISL regardless of the motion strength.
3. Several turbulence scales are identified by EMD. The conventional $-5/3$ law is observed by the peaks of power spectra density (PSD) of the IMF modes. The largest turbulence scale appears in the mode with largest order whose length scale is comparable to the TBL thickness. Hence, the momentum of the largest turbulence scales is entrained from the atmospheric boundary layer (ABL). The largest amplitude fluctuation occurs

more frequently when the turbulence length scale is close to the TBL thickness.

4. A tight correlation between large and small scales is found in RSL bottom where they interact with each other via a range of turbulence processes. It thus echoes the conclusion drawn in the frequency analysis. The AM correlation coefficient between large and small scales R_{AM} is positive in RSLs and negative in ISLs, suggesting the accelerating and decelerating effect between the large- and small-scale turbulence. There is a time lag between large- and small-scale turbulence, and the large-scale turbulence leads the small-scale turbulence $0 \leq tu_\tau/\delta \leq 0.025$ with increasing height.
5. The large-scale, negative fluctuations overlap with the low-energy, small-scale fluctuations more frequently. On the contrary, the high-speed, large-scale fluctuations coincide with more energetic, small-scale fluctuations in RSLs. With increasing wall-normal distance, the increasing speed of large-scale turbulence with decreasing small-scale energy happens more frequently. In ISLs, low-energy, small-scale fluctuations accompany with the high-speed, large-scale fluctuations more frequently.

It is demonstrated that large turbulence scales (also) have a major influence even close to the ground surface, explaining the inhomogeneous flow characteristics in urban RSLs. The large-scale turbulence aids in distributing pollutants more widely, while smaller-scale eddies might affect local mixing. Thus the widely dispersed pollutant will also

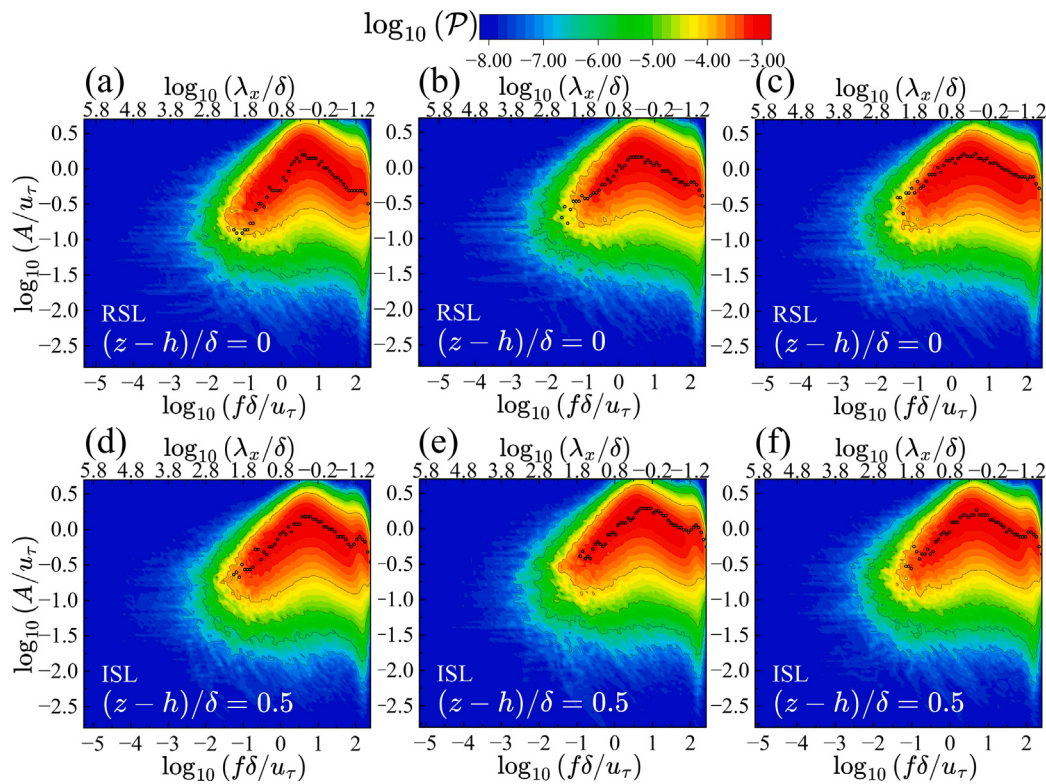


Fig. 11. JPDF of amplitude and frequency $\mathcal{P}(f, A)$ for the streamwise fluctuating velocity u'' on the: (a) and (d) 1st; (b) and (e) 2nd; together with (c) and (f) 3rd planes. The dark circles signify the most likely occurring amplitudes of streamwise fluctuating velocity $|u''|$ at different frequencies.

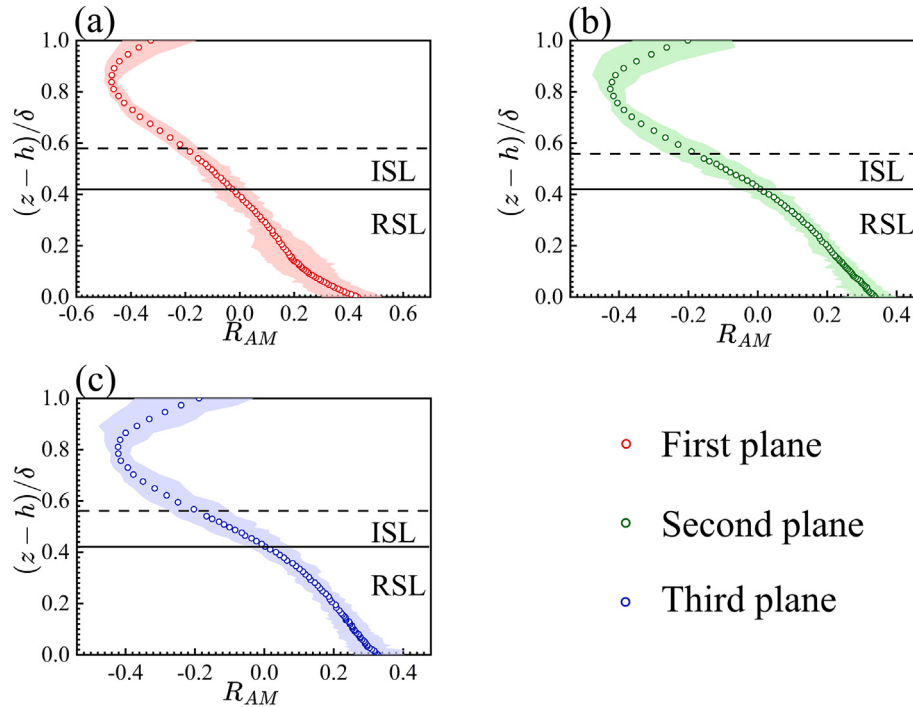


Fig. 12. Vertical profiles of amplitude modulation (AM) correlation coefficient R_{AM} of the streamwise fluctuating velocity u'' on the (a) 1st; (b) 2nd; and (c) 3rd planes. The symbols are the ensemble average and the shaded area is the variation.

have an influence on the local mixing. How the turbulence strength varies with the turbulence scales together with the interaction amid

full spectra of turbulence scales elucidate street-level ventilation and pollutant transport. The AM in RSLs elaborated above suggests the

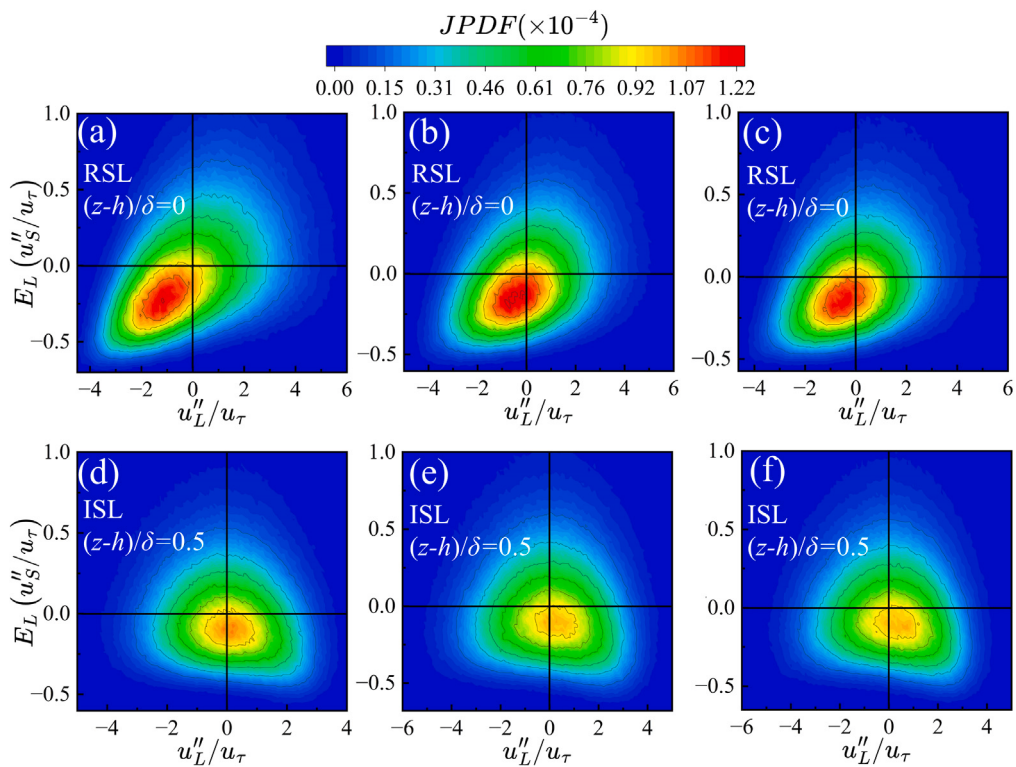


Fig. 13. JPDF of u''_L/u_τ and $E_L(u''_S/u_\tau)$ on the: (a) and (d) 1st; (b) and (e) 2nd; together with (c) and (f) 3rd planes. (a) ~ (c) are in the RSL bottom, $(z - h)/\delta = 0$; (d) ~ (f) are in the ISL, $(z - h)/\delta = 0.5$.

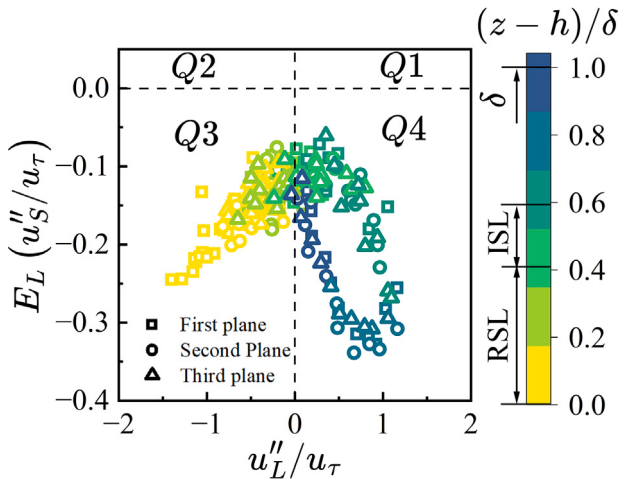


Fig. 14. Distribution of peaked JPDF expressed as a function of u''_L and $E_L(u''_S)$.

interaction between large and small scales. It would help enrich our understanding of winds over cities as well as improve the prediction of pedestrian-level winds and ventilation. The outcome would be interesting to the communities of wind loading and structurally engineering.

The ABL is seldom isothermal, which, however, is technically challenging to be modeled in laboratory-scale wind tunnels. Generally, stable and unstable stratification suppresses and enhances transport, respectively. This study is limited to neutrally stratified ABL because of the laboratory infrastructure. In case of thermal stratification, the Reynolds number and Richardson number are the two dimensionless

groups to fulfill kinematic and dynamic similarity. Matching both dimensionless groups simultaneously is an experimental hurdle. Field measurements are thus able to shed some light on the turbulence in stratified ABL.

CRediT authorship contribution statement

Fei Li: Writing – original draft, Visualization, Validation, Software, Methodology, Investigation, Formal analysis, Data curation. **Ruiqi Wang:** Writing – review & editing, Validation, Methodology, Investigation, Formal analysis, Data curation. **Guoliang Chen:** Writing – review & editing, Validation, Methodology, Investigation, Formal analysis, Data curation. **Ziwei Mo:** Writing – review & editing, Data curation. **Naoki Ikegaya:** Writing – review & editing. **Chun-Ho Liu:** Writing – review & editing, Writing – original draft, Supervision, Resources, Project administration, Funding acquisition, Conceptualization.

Declaration of competing interest

The authors declare the following financial interests/personal relationships which may be considered as potential competing interests: Chun-Ho LIU reports financial support was provided by Hong Kong (HK) Research Grants Council (RGC). If there are other authors, they declare that they have no known competing financial interests or personal relationships that could have appeared to influence the work reported in this paper.

Acknowledgments

This study is partly supported by the Hong Kong (HK) Research Grants Council (RGC) Theme-based Research Scheme (TRS) T24-504/17-N, the RGC Collaborative Research Fund (CRF) C7064-18G and C5108-20G, as well as the RGC General Research Fund (GRF) 17209819 and 17211322. The technical support from Mr. Vincent K.W. Lo is appreciated.

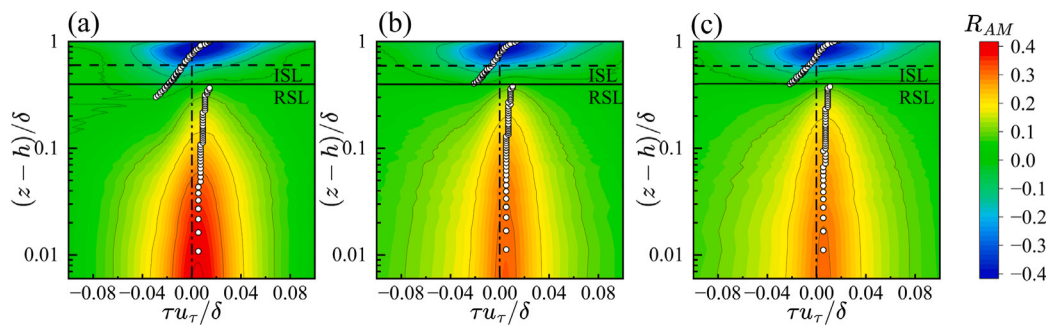


Fig. 15. Shaded contours of amplitude modulation (AM) correlation coefficient $R_{AM}(\tau)$ between large and small scales with dimensionless time lag $\tau u_\tau / \delta$ at different height $(z - h) / \delta$ on the (a) 1st; (b) 2nd; and (c) 3rd planes. The solid and dashed lines represent the RSL top and ISL top, respectively. The white dots mark the ridge of the contours.

Appendix. Empirical Mode Decomposition (EMD) and Hilbert transform

Empirical mode decomposition (EMD) and Hilbert transform are introduced in this appendix. Given an arbitrary one-dimensional (1D), mono-component signal $\phi(t)$, the algorithm of standard EMD is summarized as follows [49–51,58]:

1. Identify all the local extrema of the time-series signal $\phi(t)$. Interpolate the local minima $\epsilon_{min}(t)$ and the local maxima $\epsilon_{max}(t)$ for the signal envelope.
2. Calculate the local mean $\theta(t) = (\epsilon_{min}(t) + \epsilon_{max}(t)) / 2$.
3. Subtract the local mean from the signal to obtain the modulated oscillation $\kappa(t) = \phi(t) - \theta(t)$.
4. If $\kappa(t)$ satisfies the stopping criterion, it is an IMF so $I(t) = \theta(t)$, otherwise set $\phi(t) = \kappa(t)$ and repeat the calculation from step 1.

By repeating the steps above, the number of signal extrema decreases. The iteration ends when only one extremum remains, or the residual remains constant so no more IMF is generated. The signal

$$\phi(t) = \sum_{i=1}^N I_i(t) + \mathcal{R}(t) \quad (\text{A.1})$$

is finally written as the linear combination of N number of IMFs $I_i(t)$ and the residual $\mathcal{R}(t)$.

After the signal decomposition by EMD, the Hilbert spectral analysis (HSA) is used to calculate the instantaneous frequency $f_i(t)$ and the instantaneous amplitude $A_i(t)$ of individual IMFs [57,58]. It is associated with the Hilbert transform

$$\tilde{I}_i(t) = \frac{1}{\pi} \int_{-\infty}^{+\infty} \frac{I_i(\tau)}{t - \tau} d\tau \quad (\text{A.2})$$

and the analytic signal is written as

$$\begin{aligned} z &= I_i(t) + j\tilde{I}_i(t) \\ &= A_i(t)e^{j\theta_i(t)} \end{aligned} \quad (\text{A.3})$$

where $\theta_i(t)$ ($= \tan^{-1}(\tilde{I}_i(t) / I_i(t))$) is the instantaneous phase of IMF oscillation [73]. Neglecting the residual $\mathcal{R}(t)$, the original signal can be reconstructed by the real part of the analytical signal

$$\phi(t) = \operatorname{Re} \left(\sum_{i=1}^N A_i(t) e^{j\theta_i(t)} \right). \quad (\text{A.4})$$

The Hilbert spectrum of each IMF $H_i(f_i, t)$, which represents the energy of I_i in the time-frequency domain, is defined as the square of the amplitude, and

$$\begin{aligned} f_i(t) &= d\theta_i(t)/dt \\ &= d \left(\tan^{-1} \frac{\tilde{I}_i(t)}{I_i(t)} \right) / dt \end{aligned} \quad (\text{A.5})$$

the instantaneous frequency. The Hilbert marginal spectrum is then expressed as

$$H_i(f_i) = \int_0^\infty H_i(f_i, t) dt \quad (\text{A.6})$$

that depicts the energy density of I_i at frequency f_i [51,57,58].

Afterward, the joint probability density function (JPDF) $P(f_i, A_i)$ for the frequency f_i and the amplitude A_i of I_i are derived. The Hilbert marginal spectrum of each IMF is also calculated by the JPDF

$$H_i(f_i) = \int_0^\infty p(f_i, A_i) A_i^2 dt. \quad (\text{A.7})$$

The energy information in the frequency-amplitude domain is then obtained.

Data availability

Data will be made available on request.

References

- [1] Liu Huizhi, Liang Bin, Zhu Fengrong, Zhang Boyin, Sang Jianguo, A laboratory model for the flow in urban street canyons induced by bottom heating, *Adv. Atmos. Sci.* 20 (2003) 554–564.
- [2] K. Ahmad, M. Khare, K.K. Chaudhry, Wind tunnel simulation studies on dispersion at urban street canyons and intersections—a review, *J. Wind Eng. Ind. Aerodyn.* 93 (9) (2005) 697–717.
- [3] Ziwei Mo, Chun-Ho Liu, A wind tunnel study of ventilation mechanism over hypothetical urban roughness: The role of intermittent motion scales, *Build. Environ.* 135 (2018) 94–103.
- [4] Yixin Liu, Chun-Ho Liu, Guy P Brasseur, Christopher YH Chao, Wavelet analysis of the atmospheric flows over real urban morphology, *Sci. Total Environ.* 859 (2023) 160209.
- [5] M.R. Raupach, B.J. Legg, The uses and limitations of flux-gradient relationships in micrometeorology, in: *Developments in Agricultural and Managed Forest Ecology*, Vol. 13, Elsevier, 1984, pp. 119–131.
- [6] J.R. Garratt, Flux profile relations above tall vegetation, *Q. J. R. Meteorol. Soc.* 104 (439) (1978) 199–211.
- [7] John J. Finnigan, Roger H. Shaw, Edward G. Patton, Turbulence structure above a vegetation canopy, *J. Fluid Mech.* 637 (2009) 387–424.
- [8] Yat-Kiu Ho, Chun-Ho Liu, A wind tunnel study of flows over idealised urban surfaces with roughness sublayer corrections, *Theor. Appl. Climatol.* 130 (2017) 305–320.
- [9] Yat-Kiu Ho, Chun-Ho Liu, Street-level ventilation in hypothetical urban areas, *Atmosphere* 8 (2017) 124.
- [10] Ziwei Mo, Chun-Ho Liu, Yat-Kiu Ho, Roughness sublayer flows over real urban morphology: A wind tunnel study, *Build. Environ.* 188 (2021) 107463.
- [11] Zuzana Kluková, Štěpán Nosek, Vladimír Fuka, Zbyněk Jaňour, Hana Chaloupecká, Jana Čoubalová, The combining effect of the roof shape, roof-height non-uniformity and source position on the pollutant transport between a street canyon and 3D urban array, *J. Wind Eng. Ind. Aerodyn.* 208 (2021) 104468.
- [12] Ian N. Harman, John J. Finnigan, A simple unified theory for flow in the canopy and roughness sublayer, *Bound.-Layer Meteorol.* 123 (2007) 339–363.
- [13] Runmin Zhao, Junjie Liu, Nan Jiang, Sumei Liu, Wind tunnel and numerical study of outdoor particle dispersion around a low-rise building model, *Archit. Intell.* 3 (1) (2024) 1.

- [14] Lior Shig, Valery Babin, Ron Shnapp, Eyal Fattal, Alex Liberzon, Yardena Bohbot-Raviv, Flow and turbulence statistics of a two-height canopy model in a wind tunnel, *Bound.-Layer Meteorol.* 187 (3) (2023) 591–617.
- [15] AA Aliabadi, M Moradi, D Clement, WD Lubitz, B Gharabaghi, Flow and temperature dynamics in an urban canyon under a comprehensive set of wind directions, wind speeds, and thermal stability conditions, *Environ. Fluid Mech.* 19 (2019) 81–109.
- [16] Amir A. Aliabadi, Mohsen Moradi, Ryan A.E. Byerlay, The budgets of turbulence kinetic energy and heat in the urban roughness sublayer, *Environ. Fluid Mech.* 21 (4) (2021) 843–884.
- [17] Nicholas Hutchins, Ivan Marusic, Large-scale influences in near-wall turbulence, *Phil. Trans. R. Soc. A* 365 (1852) (2007) 647–664.
- [18] Matteo Bernardini, Sergio Pirozzoli, Inner/outer layer interactions in turbulent boundary layers: a refined measure for the large-scale amplitude modulation mechanism, *Phys. Fluids* 23 (6) (2011).
- [19] Eda Dogan, Ramis Örlü, Davide Gatti, Ricardo Vinuesa, Philipp Schlatter, Quantification of amplitude modulation in wall-bounded turbulence, *Fluid Dyn. Res.* 51 (1) (2019) 011408.
- [20] I. Marusic, R. Mathis, N. Hutchins, Predictive model for wall-bounded turbulent flow, *Science* 329 (5988) (2010) 193–196.
- [21] Romain Mathis, Nicholas Hutchins, Ivan Marusic, A predictive inner–outer model for streamwise turbulence statistics in wall-bounded flows, *J. Fluid Mech.* 681 (2011) 537–566.
- [22] James M. Wallace, Helmut Eckelmann, Robert S. Brodkey, The wall region in turbulent shear flow, *J. Fluid Mech.* 54 (1) (1972) 39–48.
- [23] Robert S. Brodkey, James M. Wallace, Helmut Eckelmann, Some properties of truncated turbulence signals in bounded shear flows, *J. Fluid Mech.* 63 (2) (1974) 209–224.
- [24] Connie A Chapman, Ian J Walker, Patrick A Hesp, Bernard O Bauer, Robin GD Davidson-Arnott, Turbulent Reynolds stress and quadrant event activity in wind flow over a coastal foredune, *Geomorphology* 151 (2012) 1–12.
- [25] W.W. Willmarth, S.S. Lu, Structure of the Reynolds stress near the wall, *J. Fluid Mech.* 55 (1) (1972) 65–92.
- [26] S.S. Lu, W.W. Willmarth, Measurements of the structure of the Reynolds stress in a turbulent boundary layer, *J. Fluid Mech.* 60 (3) (1973) 481–511.
- [27] Hiroji Nakagawa, Iehisa Nezu, Prediction of the contributions to the Reynolds stress from bursting events in open-channel flows, *J. Fluid Mech.* 80 (1) (1977) 99–128.
- [28] R.A. Antonia, Conditional sampling in turbulence measurement, *Annu. Rev. Fluid Mech.* 13 (1) (1981) 131–156.
- [29] Chun-Ho Liu, Chi-To Ng, Colman CC Wong, A theory of ventilation estimate over hypothetical urban areas, *J. Hazard. Mater.* 296 (2015) 9–16.
- [30] Ziwei Mo, Chun-Ho Liu, Hei-Lim Chow, Ming-Kei Lam, Yiu-Him Lok, See-Wah Ma, Fu-Lam Wong, Pik-Yan Yip, Roughness sublayer over vegetation canopy: A wind tunnel study, *Agricul. Forest. Meteorol.* 316 (2022) 108880.
- [31] Lan Yao, Chun-Ho Liu, Ziwei Mo, Wai-Chi Cheng, Guy P Brasseur, Christopher YH Chao, Statistical analysis of the organized turbulence structure in the inertial and roughness sublayers over real urban area by building-resolved large-eddy simulation, *Build. Environ.* 207 (2022) 108464.
- [32] Xin Shao, Ning Zhang, Zhen Peng, Kun Zhao, Yanhong Luo, Xiaoquan Song, Observed surface drag coefficient under high wind speed conditions and the relationship with coherent structures, *J. Geophys. Res.: Atmos.* 127 (3) (2022) e2021JD035301.
- [33] W. Zhu, R. Van Hout, J. Katz, PIV measurements in the atmospheric boundary layer within and above a mature corn canopy. Part II: Quadrant-hole analysis, *J. Atmos. Sci.* 64 (8) (2007) 2825–2838.
- [34] Stephen J Kline, William C Reynolds, FA Schraub, PW Runstadler, The structure of turbulent boundary layers, *J. Fluid Mech.* 30 (4) (1967) 741–773.
- [35] Edward Robert Corino, Robert S. Brodkey, A visual investigation of the wall region in turbulent flow, *J. Fluid Mech.* 37 (1) (1969) 1–30.
- [36] Kateralli R. Sreenivasan, R.A. Antonia, The phenomenology of small-scale turbulence, *Annu. Rev. Fluid Mech.* 29 (1) (1997) 435–472.
- [37] Javier Jiménez, The largest scales of turbulent wall flows, *CTR Annu. Res. Briefs* 137 (1998) 54.
- [38] Qi Li, Elie Bou-Zeid, Contrasts between momentum and scalar transport over very rough surfaces, *J. Fluid Mech.* 880 (2019) 32–58.
- [39] Mikko Auvinen, Simone Boi, Antti Hellsten, Topi Tanhuapää, Leena Järvi, Study of realistic urban boundary layer turbulence with high-resolution large-eddy simulation, *Atmosphere* 11 (2) (2020) 201.
- [40] H.B. Lin, J.Y. Fu, Z.R. Shu, Q.S. Li, P.W. Chan, Y.C. He, Spectral characteristics of surface atmosphere in range of macroscale to microscale at Hong Kong, *J. Wind Eng. Ind. Aerodyn.* 208 (2021) 104446.
- [41] Bharathram Ganapathisubramani, Ellen K Longmire, Ivan Marusic, Characteristics of vortex packets in turbulent boundary layers, *J. Fluid Mech.* 478 (2003) 35–46.
- [42] Javier Jiménez, Juan C. Del Alamo, Oscar Flores, The large-scale dynamics of near-wall turbulence, *J. Fluid Mech.* 505 (2004) 179–199.
- [43] Nicholas Hutchins, Ivan Marusic, Evidence of very long meandering features in the logarithmic region of turbulent boundary layers, *J. Fluid Mech.* 579 (2007) 1–28.
- [44] M. Guala, S.E. Hommema, R.J. Adrian, Large-scale and very-large-scale motions in turbulent pipe flow, *J. Fluid Mech.* 554 (2006) 521–542.
- [45] J.G. Chen, S.L. Tang, T.M. Zhou, Y. Zhou, Very-large-scale motions in the turbulent cylinder wake, *Phys. Fluids* 34 (6) (2022).
- [46] S.J. Loutridis, Damage detection in gear systems using empirical mode decomposition, *Eng. Struct.* 26 (12) (2004) 1833–1841.
- [47] J. Chen, You Lin Xu, R.C. Zhang, Modal parameter identification of Tsing Ma suspension bridge under typhoon victor: EMD-HT method, *J. Wind Eng. Ind. Aerodyn.* 92 (10) (2004) 805–827.
- [48] J.I. Salisbury, Mark Wimbush, Using modern time series analysis techniques to predict ENSO events from the SOI time series, *Nonlinear Process. Geophys.* 9 (3/4) (2002) 341–345.
- [49] Yongxiang Huang, François G Schmitt, Zhiming Lu, Yulu Liu, Analysis of experimental homogeneous turbulence time series by Hilbert-Huang transform, in: CFM 2007-18ème Congrès Français de Mécanique, AFM, Maison de la Mécanique, 39/41 rue Louis Blanc-92400 Courbevoie, 2007.
- [50] Y.X. Huang, François G. Schmitt, Z.M. Lu, Y.L. Liu, An amplitude-frequency study of turbulent scaling intermittency using empirical mode decomposition and Hilbert spectral analysis, *Europhys. Lett.* 84 (4) (2008) 40010.
- [51] François G Schmitt, Yongxiang Huang, Zhiming Lu, Yulu Liu, Nicolas Fernandez, Analysis of velocity fluctuations and their intermittency properties in the surf zone using empirical mode decomposition, *J. Mar. Syst.* 77 (4) (2009) 473–481.
- [52] Alexander J. Smits, Beverley J. McKeon, Ivan Marusic, High-Reynolds number wall turbulence, *Annu. Rev. Fluid Mech.* 43 (2011) 353–375.
- [53] Romain Mathis, Nicholas Hutchins, Ivan Marusic, Large-scale amplitude modulation of the small-scale structures in turbulent boundary layers, *J. Fluid Mech.* 628 (2009) 311–337.
- [54] Zhanqi Tang, Nan Jiang, Scale interaction and arrangement in a turbulent boundary layer perturbed by a wall-mounted cylindrical element, *Phys. Fluids* 30 (5) (2018).
- [55] M.R. Raupach, Conditional statistics of Reynolds stress in rough-wall and smooth-wall turbulent boundary layers, *J. Fluid Mech.* 108 (1981) 363–382.
- [56] James M. Wallace, Quadrant analysis in turbulence research: history and evolution, *Annu. Rev. Fluid Mech.* 48 (2016) 131–158.
- [57] Steven R Long, NE Huang, CC Tung, ML Wu, RQ Lin, E Mollo-Christensen, Y Yuan, The Hilbert techniques: an alternate approach for non-steady time series analysis, *IEEE Geosci. Remote Sens. Soc. Lett.* 3 (1995) 6–11.
- [58] Norden E Huang, Zheng Shen, Steven R Long, Manli C Wu, Hsing H Shih, Quanan Zheng, Nai-Chyuan Yen, Chi Chao Tung, Henry H Liu, The empirical mode decomposition and the Hilbert spectrum for nonlinear and non-stationary time series analysis, *Proc. R. Soc. Lond. Ser. A Math. Phys. Eng. Sci.* 454 (1998) 903–995.
- [59] Ruiqi Wang, Chun-Ho Liu, Fei Li, Mo Ziwei, Turbulent transport mechanism in the roughness sublayers over idealized urban areas and its implication to street-level ventilation, *Sustainable Cities Soc.* 100 (2024) 105030.
- [60] Ziwei Mo, Chun-Ho Liu, Transport mechanism of urban plume dispersion, *Build. Environ.* 161 (2019) 106239.
- [61] Chun-Ho Liu, Mo Ziwei, Zhangquan Wu, Parameterization of vertical dispersion coefficient over idealized rough surfaces in isothermal conditions, *Geosci. Lett.* 5 (2018) 24.
- [62] William H. Snyder, Ian P. Castro, The critical Reynolds number for rough-wall boundary layers, *J. Wind Eng. Ind. Aerodyn.* 90 (1) (2002) 41–54.
- [63] Pietro Salizzoni, Lionel Soulhac, Patrick Mejean, Richard J Perkins, Influence of a two-scale surface roughness on a neutral turbulent boundary layer, *Bound.-Layer Meteorol.* 127 (1) (2008) 97–110.
- [64] Hong Cheng, Ian P. Castro, Near wall flow over urban-like roughness, *Bound.-Layer Meteorol.* 104 (2002) 229–259.
- [65] Michael R Raupach, Robert Anthony Antonia, Sundara Rajagopalan, Rough-wall turbulent boundary layers, *Appl. Mech. Rev.* 44 (1991) 1–25.
- [66] Xuebo Li, Tianli Bo, An application of quadrant and octant analysis to the atmospheric surface layer, *J. Wind Eng. Ind. Aerodyn.* 189 (2019) 1–10.
- [67] Michele Guala, M. Metzger, Beverley J. McKeon, Interactions within the turbulent boundary layer at high Reynolds number, *J. Fluid Mech.* 666 (2011) 573–604.
- [68] Bharathram Ganapathisubramani, Nicolas Hutchins, Jason P Monty, Daniel Chung, Ivan Marusic, Amplitude and frequency modulation in wall turbulence, *J. Fluid Mech.* 712 (2012) 61–91.
- [69] I. Jacobi, B.J. McKeon, Phase relationships between large and small scales in the turbulent boundary layer, *Exp. Fluids* 54 (2013) 1–13.
- [70] Ian Jacobi, Daniel Chung, Subrahmanyam Duvvuri, Beverley J McKeon, Interactions between scales in wall turbulence: phase relationships, amplitude modulation and the importance of critical layers, *J. Fluid Mech.* 914 (2021) A7.
- [71] I. Jacobi, B.J. McKeon, Phase-relationships between scales in the perturbed turbulent boundary layer, *J. Turbul.* 18 (12) (2017) 1120–1143.
- [72] W.J. Baars, Nicholas Hutchins, Ivan Marusic, Reynolds number trend of hierarchies and scale interactions in turbulent boundary layers, *Phil. Trans. R. Soc. A* 375 (2009) (2017) 20160077.
- [73] Leon Cohen, Time-Frequency Analysis, Vol. 778, Prentice Hall PTR Englewood Cliffs, 1995.